# POTENTIAL AND CURRENT DISTRIBUTIONS IN A CYLINDRICAL BUNDLE OF CARDIAC TISSUE

C. S. HENRIQUEZ, N. TRAYANOVA, AND R. PLONSEY
*Department of Biomedical Engineering, Duke University, Durham, North Carolina 27706*

ABSTRACT The intracellular and interstitial potentials associated with each cell or fiber in multicellular preparations carrying a uniformly propagating wave are important for characterizing the electrophysiological behavior of the preparation and in particular, for evaluating the source contributed by each fiber. The aforementioned potentials depend on a number of factors including the conductivities characterizing the intracellular, interstitial, and extracellular domains, the thickness of the tissue, and the distance (depth) of the field point from the surface of the tissue. A model study is presented describing the extracellular and interstitial potential distribution and current flow in a cylindrical bundle of cardiac muscle arising from a planar wavefront. For simplicity, the bundle is considered as a bidomain. Using typical values of conductivity, the results show that the intracellular and interstitial potential of fibers near the center of a very large bundle (>10 mm) may be approximated by the potentials of a single fiber surrounded by a limited extracellular space (a fiber in oil), hence justifying a core-conductor model. For smaller bundles, the peak interstitial potential is less than that predicted by the core-conductor model but still large enough to affect the overall source strength. The magnitude of the source strength is greatest for fibers lying near the center of the bundle and diminishes sharply for fibers within 50 $\mu$m of the surface.

## INTRODUCTION

The electric field arising from activity in a bundle of fibers (either skeletal or cardiac muscle or even nerve) has often been described using the elementary model of a single isolated fiber (1–5). Typically in these descriptions, the transmembrane current is viewed as a source for the extracellular fields. The assumption that the behavior of a single fiber in isolation is the same as when associated with a large number of fibers in a closely packed array is, however, not correct. This paper presents the results of a model study of the extracellular fields arising from excitation of a multicellular preparation of cardiac muscle.

A bundle of cardiac muscle comprises tightly packed cells that are extensively coupled both longitudinally and laterally. Each cell is surrounded by an envelope of extracellular fluid (6). Deep within the preparation, the effective axial interstitial resistance is significant and will affect the electrical source strength associated with the cellular activity. The structure also helps to constrain both the intracellular and interstitial current to flow axially.

Here we describe the formulation and evaluation of the potential distribution and current flow in a cylindrical bundle of cardiac tissue surrounded by an extensive volume conductor. For simplicity, the bundle is described as a cylindrical bidomain, a model originally developed by Roth and Wikswo (7) to aid in interpreting magnetic field measurements of cardiac muscle. In a related study to ours, Plonsey and Barr (8) used the bidomain approximation to examine the interstitial potential in a less realistic geometry of a semi-infinite block.

## CYLINDRICAL BUNDLE MODEL

### Bidomain Approximation

The bidomain model (9) is a macroscopic representation of cardiac tissue that considers the structure to consist of two continuous domains, intracellular and interstitial, superimposed in space and separated by a membrane distributed throughout the volume. Consistent with a continuum description, the effect of the discrete cellular nature on propagation is ignored. The results from Henriquez and Plonsey (10) and Rudy and Quan (11) support this approximation since it is shown that the influence of the intercellular junctions (apart from the contribution of the junctional resistance to the total intracellular resistance) on waveshape and velocity is small for normal myocardium. The two domains are linked through the transmembrane current; the outflow from one region must equal the inflow to the other. At any point the transmembrane potential, $V_m$, is the difference between the intracellular and interstitial potentials. The parameters characterizing each continuous domain are averaged values over a volume of many cells. Because of the geometry of the interconnections and the structure of the cells, both the intracellular and interstitial bidomain conductivities are anisotropic.

---

Dr. Trayanova is a Visiting Scholar to Duke University from the Bulgarian Academy of Science, Sofia, Bulgaria.

## Geometry

We consider a cylindrical bundle of cardiac tissue, infinite in extent and with a radius $a$ (Fig. 1), surrounded by an unbounded, isotropic volume conductor. Because of this geometry, we use a cylindrical coordinate system $\rho$, $z$, $\theta$. The activation wavefront is assumed to be planar and propagating with uniform velocity.

The assumption that $V_m$ is constant throughout any cross-section is the same as that used by Roth and Wikswo (7) and Plonsey and Barr (8). We have adopted this assumption since it leads to a mathematical simplification. Due to the cylindrical symmetry, the potentials and currents are independent of $\theta$. As in Plonsey and Barr (8), the extracellular potential is denoted by $\Phi_o$, the interstitial potential by $\Phi_e$, and the intracellular potential by $\Phi_i$.

## Conductivities

We assume that the individual fibers are parallel to the axis of the cylindrical bidomain and that the intracellular conductivity, $\sigma_i$, is greater in the axial, $z$, direction than in the radial, $\rho$, direction (i.e., $\sigma_{iz} > \sigma_{i\rho}$; for skeletal muscle or nerve, $\sigma_{i\rho} = 0$). In addition, because of the physical structure we assumed that the interstitial conductivity, $\sigma_e$, is greater in the axial direction (i.e., $\sigma_{ez} > \sigma_{e\rho}$). Using data from Clerc (12) and assuming 80% of the total tissue volume is intracellular, the axial and radial conductivities expressed in bidomain format are given below:

$$g_{iz} = \sigma_{iz} f_i = 1.94 \times 10^{-1}\ \text{S/m}$$

$$g_{ez} = \sigma_{ez} f_e = 4.17 \times 10^{-1}\ \text{S/m} \quad (1)$$

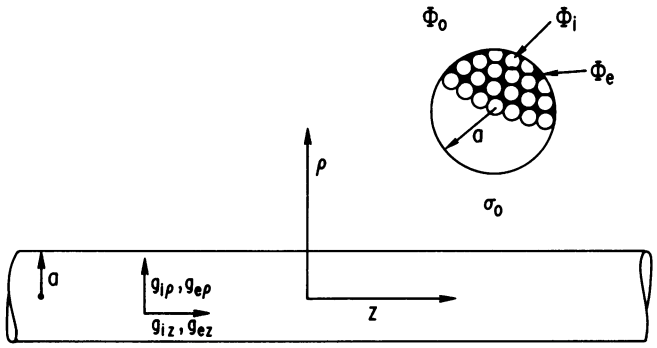


FIGURE 1 Schematic representation of the geometry of the cylindrical bidomain of a bundle of cardiac fibers surrounded by an extensive volume conductor of conductivity $\sigma_o$. The intracellular domain is denoted by the subscript i, the interstitial domain (extracellular space within the tissue) is denoted by the subscript e, the extracellular domain is denoted by the subscript o. Due to the cylindrical symmetry, the potentials and currents are functions of only $\rho$ and $z$. The fiber is assumed to have infinite length and a radius, $a$. The interstitial and intracellular conductivity values are scaled into bidomain conductivities ($g$'s) to reflect the fact that each domain is assumed to occupy the entire volume of the bundle. The actual bundle (which the bidomain model approximates) is assumed to be composed of multiple and similar fibers lying parallel to the axis of the cylinder. A cross-section of the bundle, revealing the latter structure, is shown in the inset.

$$g_{i\rho} = \sigma_{i\rho} f_i = 2.21 \times 10^{-2}\ \text{S/m}$$

$$g_{e\rho} = \sigma_{e\rho} f_e = 1.57 \times 10^{-1}\ \text{S/m}, \quad (2)$$

where $f_i$ and $f_e$ are the fractions of the total cross-sectional area occupied by the intracellular and interstitial domains, respectively. The introduction of $f_i$ and $f_e$ is necessary since both the intracellular and interstitial domains are defined to occupy the total tissue volumes.[1] The extracellular medium is assumed to have a conductivity $\sigma_0 = 2.0$ S/m, similar to that of Tyrode's solution. The values of conductivity were chosen to be consistent with those used by Plonsey and Barr, to more easily compare results.

## Interstitial and Extracellular Potentials

The extracellular potential $\Phi_o$ satisfies Laplace's equation.

$$\nabla^2 \Phi_o = 0, \quad (3)$$

and will be described in a cylindrical coordinate system ($\rho$, $z$, $\theta$), while the interstitial potential $\Phi_e$ satisfies Poisson's equation (8)

$$\nabla^2 \Phi_e = -\frac{g_{iz}}{g_{iz} + g_{ez}} \nabla^2 V_m \quad (4)$$

in the transformed cylindrical coordinate system ($R$, $Z$, $\theta$) where

$$R = q\rho \quad (5)$$

$$Z = z \quad (6)$$

and

$$q = \left(\frac{g_{iz} + g_{ez}}{g_{i\rho} + g_{e\rho}}\right)^{1/2}. \quad (7)$$

The classical solution for Eq. 3 is

$$\Phi_o = \int_{-\infty}^{\infty} A(k) K_0(|k|\rho) e^{-jkz}\, dk \quad (8)$$

for $\rho > a$, where $a$ is the radius of the cylinder, and $K_0$ is the modified Bessel function of the second kind and zero order (arising from axial symmetry).

The solution of Eq. 4 is a sum of the general solution of the Laplace's equation, $\nabla^2 \Phi_e = 0$, and the particular solution of Eq. 4:

$$\Phi_e = \int_{-\infty}^{\infty} B(k) I_0(|k|R) e^{-jkz}\, dk - \frac{g_{iz}}{g_{iz} + g_{ez}} V_m(z) \quad (9)$$

for $\rho < a$ (inside the cylinder). Here $I_0$ is the modified Bessel functions of zero order and first kind.

Applying the boundary conditions of continuity of

[1]The effective area for current flow in the transverse intracellular vs. transverse interstitial regions is difficult to estimate and we have simply taken this to be given by $f_i : f_e$, the same as for longitudinal flow where the aforementioned ratio corresponds to the relative cross-sectional areas.

potential,

$$\Phi_e(R, Z) = \Phi_o(\rho, z) \tag{10}$$

and continuity of the radial current

$$g_{i\rho}\frac{\partial \Phi_i}{\partial \rho} + g_{e\rho}\frac{\partial \Phi_e}{\partial \rho} = \sigma_o \frac{\partial \Phi_o}{\partial \rho} \tag{11}$$

at any point on the surface of the tissue ($\rho = a$), the coefficients $A(k)$ and $B(k)$ can be found. As noted by Roth and Wikswo (7), the boundary condition given in Eq. 11 differs from that given by Tung (9) and used by Plonsey and Barr (8), namely,

$$g_{e\rho}\frac{\partial \Phi_e}{\partial \rho} = \sigma_o \frac{\partial \Phi_o}{\partial \rho}. \tag{12}$$

The two are compatible only if the contribution of the radial component of the intracellular current density to the total extracellular current density is negligible at the surface. Rewriting Eq. 11 in terms of $\Phi_e$

$$g_{i\rho}\frac{\partial V_m}{\partial \rho} + (g_{i\rho} + g_{e\rho})\frac{\partial \Phi_e}{\partial \rho} = \sigma_o \frac{\partial \Phi_o}{\partial \rho} \tag{13}$$

reveals that the actual difference between the conditions stated in Eqs. 11 and 12 is small provided that $\partial V_m/\partial \rho$ is zero (as is the case here) and $g_{i\rho} \ll g_{e\rho}$ (typically true for cardiac muscle).

Using the more exact boundary conditions, Eqs. 10 and 11, the solutions for $\Phi_o$ and $\Phi_e$ have the following forms:[2]

$$\Phi_o(\rho, z) = -\frac{g_{iz}}{q}\mathcal{F}^{-1}[\mathcal{V}_m(k)H_1(k)] \tag{14}$$

$$\Phi_e(\rho, z) = \sigma_o \frac{g_{iz}}{g_{iz} + g_{ez}}\mathcal{F}^{-1}[\mathcal{V}_m(k)H_2(k)] - \frac{g_{iz}}{g_{iz} + g_{ez}}V_m(z), \tag{15}$$

where the operator $\mathcal{F}$ denotes a Fourier transformation and $\mathcal{F}^{-1}$ its inverse, i.e.,

$$\mathcal{F}[V_m(z)] = \mathcal{V}_m(k) = \int_{-\infty}^{\infty} V_m(z)e^{jkz}\,dz \tag{16}$$

$$\mathcal{F}^{-1}[\mathcal{V}_m(k)] = V_m(z) = \frac{1}{2\pi}\int_{-\infty}^{\infty} \mathcal{V}_m(k)e^{-jkz}\,dk. \tag{17}$$

The "filter" functions $H_1(k)$ and $H_2(k)$ are defined as

$$H_1(k) = \frac{I_1(|k|qa)\,K_0(|k|\rho)}{[\sigma_o I_o(|k|qa)K_1(|k|a) + q(g_{e\rho} + g_{i\rho})I_1(|k|qa)K_0(|k|a)]} \tag{18}$$

$$H_2(k) = \frac{K_1(|k|a)I_0(|k|q\rho)}{[\sigma_o I_o(|k|qa)K_1(|k|a) + q(g_{e\rho} + g_{i\rho})I_1(|k|qa)K_0(|k|a)]}. \tag{19}$$

## Current Densities

The interstitial and extracellular current densities can be calculated from the gradient of the potentials $\Phi_o$ and $\Phi_e$. In the extracellular space, the transverse and longitudinal current densities have the following form:

$$J_{o\rho}(\rho, z) = -\sigma_o \frac{\partial \Phi_o(z)}{\partial \rho} = -\sigma_o \frac{g_{iz}}{q}\mathcal{F}^{-1}\,[|k|\mathcal{V}_m(k)H_1'(k)] \tag{20}$$

and

$$J_{oz}(\rho, z) = -\sigma_o \frac{\partial \Phi_o(z)}{\partial z} = \sigma_o \frac{g_{iz}}{q}\mathcal{F}^{-1}\left[\mathcal{F}\left(\frac{\partial V_m}{\partial z}\right)H_1(k)\right]. \tag{21}$$

For the "filter" function $H_1'(k)$ introduced in Eq. 20 we have

$$H_1'(k) = \frac{I_1(|k|qa)K_1(|k|\rho)}{[\sigma_o I_o(|k|qa)K_1(|k|a) + q(g_{e\rho} + g_{i\rho})I_1(|k|qa)K_0(|k|a)]}. \tag{22}$$

Inside the cylinder the transverse and longitudinal interstitial current densities can be expressed as follows:

$$J_{e\rho}(\rho, z) = -g_{e\rho}\frac{\partial \Phi_e(z)}{\partial \rho} = -q\sigma_o \frac{g_{e\rho}g_{iz}}{g_{iz} + g_{ez}}\mathcal{F}^{-1}\,[|k|\mathcal{V}_m(k)H_2'(k)] \tag{23}$$

$$J_{ez}(\rho, z) = -g_{ez}\frac{\partial \Phi_e(z)}{\partial z} = -\sigma_o \frac{g_{ez}g_{iz}}{g_{iz} + g_{ez}} \cdot \mathcal{F}^{-1}\left[\mathcal{F}\left(\frac{\partial V_m}{\partial z}\right)H_2(k)\right] + \frac{g_{iz}\,g_{ez}}{g_{iz} + g_{ez}}\frac{\partial V_m(z)}{\partial z}, \tag{24}$$

where the "filter" function $H_2'$ is the following:

$$H_2'(k) = \frac{K_1(|k|a)I_1(|k|q\rho)}{[\sigma_o I_o(|k|qa)K_1(|k|a) + q(g_{e\rho} + g_{i\rho})I_1(|k|qa)K_0(|k|a)]}. \tag{25}$$

The second term in the equation for $J_{ez}$ is the "core-conductor term," the longitudinal current density according to the core-conductor model.

## Asymptotic Expressions for the Interstitial Potential

In general, the filter function $H_2(k)$ (Eq. 18) is bell-shaped. As the bundle radius increases, $H_2(k)$ becomes narrower in extent (see Appendix) and in the limit ($a \to \infty$), the filter function at the axis ($\rho = 0$) is

$$H_2(k) = \begin{cases} 0 & k \neq 0; \\ \dfrac{1}{\sigma_o} & k = 0. \end{cases} \tag{26}$$

[2]The expressions for potentials are equivalent to those given by Roth and Wikswo (7), but the form is different. The equation for $\Phi_e$ emphasizes the deviation of the interstitial potential from the limiting value it would have in a bundle of infinite radius. This limiting expression (second term in Eq. 15) corresponds to the (one-dimensional) linear core-conductor solution (to be discussed).

For an infinitely thick bundle, the first term of Eq. 15 goes to zero and the interstitial potential at the axis of the bundle is exactly equal to the potential given by the core-conductor expression,

$$\Phi_e(0,z) = -\frac{g_{iz}}{g_{iz} + g_{ez}} V_m(z). \tag{27}$$

At the surface ($\rho = a$) of the infinitely thick bundle, the function $H_2(k)$ is given by

$$H_2(k) = \begin{cases} \dfrac{1}{\sigma_o + q(g_{e\rho} + g_{i\rho})} & k \neq 0; \\ \dfrac{1}{\sigma_o} & k = 0. \end{cases} \tag{28}$$

Thus the surface potential for a bundle with $a \rightarrow \infty$ approaches:

$$\Phi_o(a,z) = -\frac{g_{iz}}{q}\frac{1}{\sigma_o + q(g_{ep} + g_{i\rho})} V_m(z). \tag{29}$$

## Asymptotic Expressions for the Longitudinal Interstital Current Density

Using an analogous approach to that used above for the interstitial potentials, the interstitial longitudinal current density at the axis ($\rho = 0$) of an infinitely thick bundle can be obtained. Using Eqs. 24 and 26,

$$J_{ez}(0,z) = \frac{g_{ez}g_{iz}}{g_{iz} + g_{ez}}\frac{\partial V_m(z)}{\partial z}. \tag{30}$$

The longitudinal current density is equal to the "ideal" core-conductor current density.

From Eq. 28, the asymptotic interstitial longitudinal current density at the surface ($a \rightarrow \infty$) is given by

$$J_{ez}(a,z) = \frac{1}{q}\frac{g_{ez}g_{iz}}{\sigma_o + q(g_{ep} + g_{i\rho})}\frac{\partial V_m(z)}{\partial z}. \tag{31}$$

We expect the surface longitudinal current density to have the same shape as that at the axis, but with a smaller amplitude.

## Current Flow Lines

The current flow lines are tangential to the vector of the current density at any point in the conducting medium. In accordance with this definition

$$\frac{dz}{J_z} = \frac{d\rho}{J_\rho} = dl, \tag{32}$$

where $J_z$ and $J_\rho$ are the longitudinal and radial current densities either in the interstitial or in the extracellular space, and $l$ is the parameter in the parametric representation of the current flow line:

$$z = z(l) \quad , \quad \rho = \rho(l). \tag{33}$$

The following system of differential equations is used to calculate the current flow lines in the interstitial domain

$$\frac{dz}{dl} = J_{ez}(\rho, z) \quad , \quad \frac{d\rho}{dl} = J_{ep}(\rho, z), \tag{34}$$

and in the extracellular domain

$$\frac{dz}{dl} = J_{oz}(\rho, z) \quad , \quad \frac{d\rho}{dl} = J_{o\rho}(\rho, z). \tag{35}$$

# SINGLE FIBER MODEL

## Single Fiber in Unbounded Volume Conductor

A common approach to modeling an entire bundle of fibers is to replace the bundle by a large single fiber with a diameter equal to that of the bundle but assign a spatial transmembrane distribution to be that of a typical component fiber inside the bundle (4). Viewing the bundle as a large single fiber in an unbounded volume conductor is equivalent to viewing the bundle as a bidomain, provided that certain conditions are satisfied. In a single fiber (13),

$$\Phi_o^s(\rho, z) = -\sigma_i^s \mathcal{F}^{-1}[\mathcal{V}_m(k)H_1^s(k)] \tag{36}$$

$$\Phi_i^s(\rho, z) = \sigma_o^s \mathcal{F}^{-1}[\mathcal{V}_m(k)H_2^s(k)], \tag{37}$$

where

$$H_1^s(k) = \frac{I_1(|k|a)K_0(|k|\rho)}{\sigma_o^s I_0(|k|a)K_1(|k|a) + \sigma_i^s I_1(|k|a)K_0(|k|a)} \tag{38}$$

$$H_2^s(k) = \frac{K_1(|k|a)I_0(|k|\rho)}{\sigma_o^s I_0(|k|a)K_1(|k|a) + \sigma_i^s I_1(|k|a)K_0(|k|a)}, \tag{39}$$

where the superscript s refers to a single fiber parameter.[3]

If $q = 1.0$ (Eq. 7), then the field of a single fiber can be converted to the field of a cylindrical bidomain by replacing $\sigma_o^s$ by $\sigma_o$, and $\sigma_i^s$ by $(g_{i\rho} + g_{ep})$ in Eqs. 38 and 39 and by multiplying the result by the scaling factor, $g_{iz}/(g_{iz} + g_{ez})$.

For the special case of a bidomain with no interstitial area, ($f_e = 0.0$), and an isotropic intracellular domain (i.e., $g_{ep} = g_{ez} = 0.0$, and $g_{i\rho} = g_{iz} = \sigma_i^s$), the equations for $\Phi_o$ (Eq. 14) and $\Phi_i$ ($\Phi_i = \Phi_o + V_m$) are identical to those of a single isolated fiber given above. Note that an equivalence also exists for $q \neq 1.0$ if $\sigma_i^s$ is replaced by $q(g_{i\rho} + g_{e\rho})$ and $\sigma_o^s$ is replaced by $\sigma_o[I_0(|k|qa)I_1(|k|a)]/[I_1(|k|qa)I_0(|k|a)]$ in the single fiber expressions and, as before, the result is multiplied by the scaling factor, $g_{iz}/(g_{iz} + g_{ez})$. A more detailed examination of this equivalence is the subject of a subsequent paper.

The extracellular single fiber potential has also been

[3]Note that the equations given in Plonsey (13) have been rewritten here to more easily compare with the equations corresponding to the cylindrical bidomain.

calculated by assuming that the transmembrane current per unit length, $i_m$, acts as a source and sets up a field such that (14)

$$\Phi_o^s = \frac{1}{4\pi\sigma_e}\int_{-\infty}^{\infty}\frac{i_m dz}{r}, \tag{40}$$

where $r$ is the distance from the source element to the field point. If the surface potential is small compared with the intracellular potential $\Phi_o^s(a, z) \ll \Phi_i^s(a, z)$, then

$$i_m \approx \pi a^2 \sigma_i \frac{\partial^2 V_m}{\partial z^2}. \tag{41}$$

## Ideal Core-Conductor Behavior

If a bundle of fibers of equal radius is surrounded by an insulating fluid such as oil, then all the currents, intracellular, interstitial, and extracellular, are constrained to flow axially. A typical fiber in such a preparation can be represented by a linear core-conductor model. One consequence of this condition is that the intracellular and extracellular potentials are proportional to the transmembrane potential (15),

$$\Phi_i = \frac{\sigma_e f_e}{\sigma_i f_i + \sigma_e f_e} V_m \tag{42}$$

$$\Phi_o = \frac{-\sigma_i f_i}{\sigma_i f_i + \sigma_e f_e} V_m. \tag{43}$$

In contrast, the intracellular and interstitial current flow in a bundle lying in an extensive volume conductor is not constrained to be uniform and axial. Hence the aforementioned relationships between $\Phi_i$ and $\Phi_o$ and $V_m$ are not valid for any fiber in the preparation except possibly for fibers near the center of a very large bundle.

## NUMERICAL METHODS

The Fourier transformations are accomplished using a Fast Fourier Transform (FFT) algorithm given by Press et al. (16). Because we use a discrete Fourier transform, we were unable to use an expression for $V_m$ that describes only the upstroke (as did Plonsey and Barr [8]), since truncation would introduce additional frequency components. Instead, we used the following analytic expression for $V_m(z)$, which represents the entire spatial extent (in meters) of an idealized cardiac action potential.

$$V_m(z) = \frac{K}{2}\tanh\left[\frac{5.0}{\theta t_f}(z + \theta T_d)\right] - \frac{K}{2}\tanh\left[\frac{5.0}{\theta t_r}(z)\right], \tag{44}$$

where $K$ is the peak amplitude in millivolts, $\theta$ is the conduction velocity in meters per second, $t_f$ and $t_d$ are the durations of the falling and rising phases, respectively, in seconds, and $T_d$ is the total duration in seconds. The first term in Eq. 44 describes the repolarization phase, while the second term describes depolarization, the region of interest. We assume the following constants: $K$ = 90 mV, $\theta$ = 0.50 m/s, $t_r$ = 0.001 s, $t_f$ = 0.0125 s, and $T_d$ = 0.320 s.[4] The number 5.0 in Eq. 44 is required to produce a typical rising extent of ~0.5 mm. The function $V_m(z)$ is approximated by 32,768 samples spaced 0.01 mm apart. The spatial extent of the rising phase is shown in Fig. 2. It is important to note that for large bundle radii, the total number of samples for a given $dz$ (total axial extent to be sampled) needed to compute the interstitial potential is not determined by the non-zero extent of $V_m(z)$, but rather by the non-zero extent of $\mathcal{F}^{-1}[H_2(k)]$ in the $z$-domain (see Appendix).

The current flow lines are generated using a three-part process. First, the longitudinal and transverse current densities are computed at discrete points within the intracellular and extracellular regions of interest forming a regular two-dimensional grid. Next, bicubic spline interpolation is used to compute the coefficients for an approximating function for both the transverse and longitudinal current densities. Finally, once these functions are defined, the system of differential equations (Eqs. 34, 35) is solved using a fourth order Runge Kutta algorithm. All simulations were performed on a 32-bit Micro-Vax II (Digital Equipment Corp., Maynard, MA).

## RESULTS

We have evaluated the expressions for the extracellular and interstitial potentials and currents for bundles of small and large radius and we have selected examples that illustrate their behavior.

Fig. 3 *a* and *b* are plots of interstitial potential at different depths in bundles with radii of 0.5 and 10.0 mm, respectively. With increasing depth in both bundles, the interstitial potential increases to a maximal value at the axis. The most dramatic change in peak potential occurs between the surface and a depth of 0.5 mm below the surface. Both the peak amplitude and axial extent of the potential are greater for the large diameter bidomain than for the small. The interstitial potential of the 0.5-mm bundle deviates everywhere from the ideal core-conductor potential in both shape and magnitude. In contrast, the interstitial potential at the axis of the 10-mm bidomain is approximately the core-conductor potential (see Eq. 27). This behavior is nearly maintained over the bulk of the cross-section. As predicted by Eq. 29, the shape of the surface potential of the 10-mm bundle resembles the core-conductor potential with a considerably smaller amplitude. This result is consistent with the result obtained by Plonsey and Barr (8) for a semi-infinite block of cardiac tissue. Note that because $\Phi_e$ is symmetric about 0 mV (see Appendix), the core-conductor potential was displaced by a constant (half its peak magnitude) to more easily compare waveshapes.

[4]Since repolarization is outside our region of interest, we made no attempt to accurately represent the plateau and the falling phase of the cardiac action potential analytically.

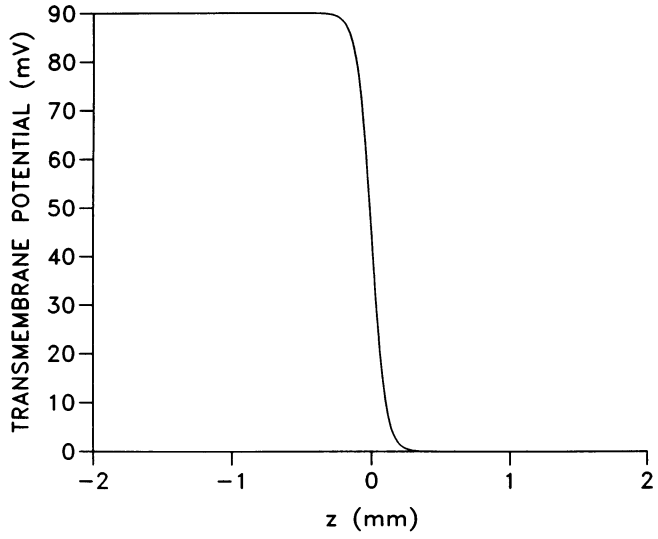


FIGURE 2 Plot of the spatial extent of the rising phase of transmembrane potential, $V_m(z)$.

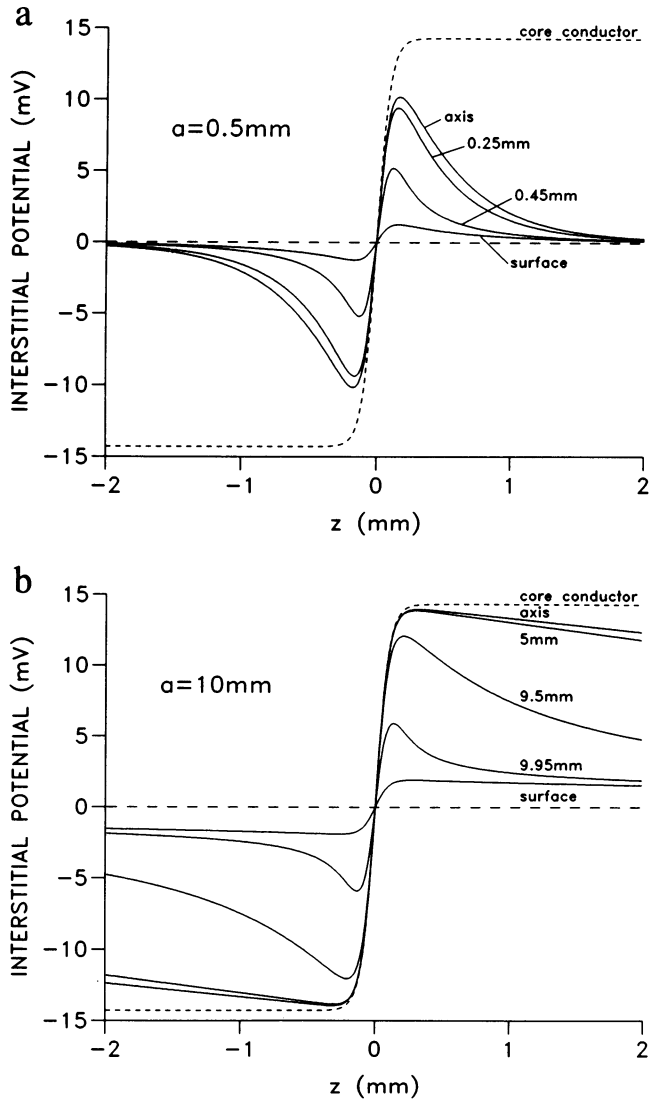


FIGURE 3 Plot of interstitial potential vs. axial distance, $z$, at different depths in a cylindrical biodomain with a radius of (*a*) 0.5 mm and (*b*) 10.0 mm.

The interstitial transverse current densities associated with the radial variation in potential for the 0.5 and 10.0 mm bundles are shown in Fig. 4. Because of the symmetry, the transverse current density is zero at the axis. In general, the current is small over the bulk of the cross-section and increases dramatically near the surface.

The longitudinal current densities at different depths in bundles with radii 0.5 and 10 mm are shown in Fig. 5. The longitudinal current density varies significantly in the region spanning the spatial extent of the upstroke of the transmembrane potential. The magnitude of this current is greatest at the axis and is relatively constant over the bulk of the cross-section. Near the surface, the longitudinal current diminishes sharply. The two small positive peaks, seen in the spatial variation of the current density at all depths of the small bundle and only near the surface of the large bundle, reflect the difference from the ideal core-conductor current density (second term of Eq. 24). Since the current density is proportional to $\partial\Phi_e/\partial z$, the peak amplitude of the longitudinal current at the axis is greater for the large bidomain and is approximately equal to the peak value predicted by Eq. 30.

The previous figures correspond to the extremes of the range of bundle radii investigated. In Fig. 6, the variation in peak interstitial potential, transverse and longitudinal current density with depth is plotted for a series of bundle radii. This figure illustrates that for bundles with radii >4 mm, the magnitudes of the potential and currents remain relatively constant over the bulk of the cross-section and decrease sharply near the surface. The radial extent over which the potential changes most (within 0.5 mm below the surface) is nearly independent of bundle size. Hence for small bidomains ($a < 2$ mm), the bulk of the cross-section cannot be characterized by a constant peak interstitial potential. The changes near the surface are sharper for the current densities than the potentials since the current are proportional to the radial and axial derivatives of the potential. In addition, the magnitudes of the peak surface potential and current densities are nearly independent of bundle radius for bundles with radii >6.0 mm.

An equipotential plot of the interstitial potential and a plot of the interstitial current flow lines for bundles with radii 0.5 and 10 mm are shown in Figs. 7 and 8, respectively. The interstitial equipotential field plot of a bundle surrounded by oil would consist entirely of parallel lines perpendicular to the axis. For a bundle in an extensive volume conductor, this ideal core-conductor behavior is seen only near the axis (0 mm) of the large bundle. A crest in the potential is clearly visible just outside the active region corresponding to rapid rising phase of $V_m(z)$. The directional nature of the electric field is evident in the plot of the current flow lines. The current flow lines, as plotted

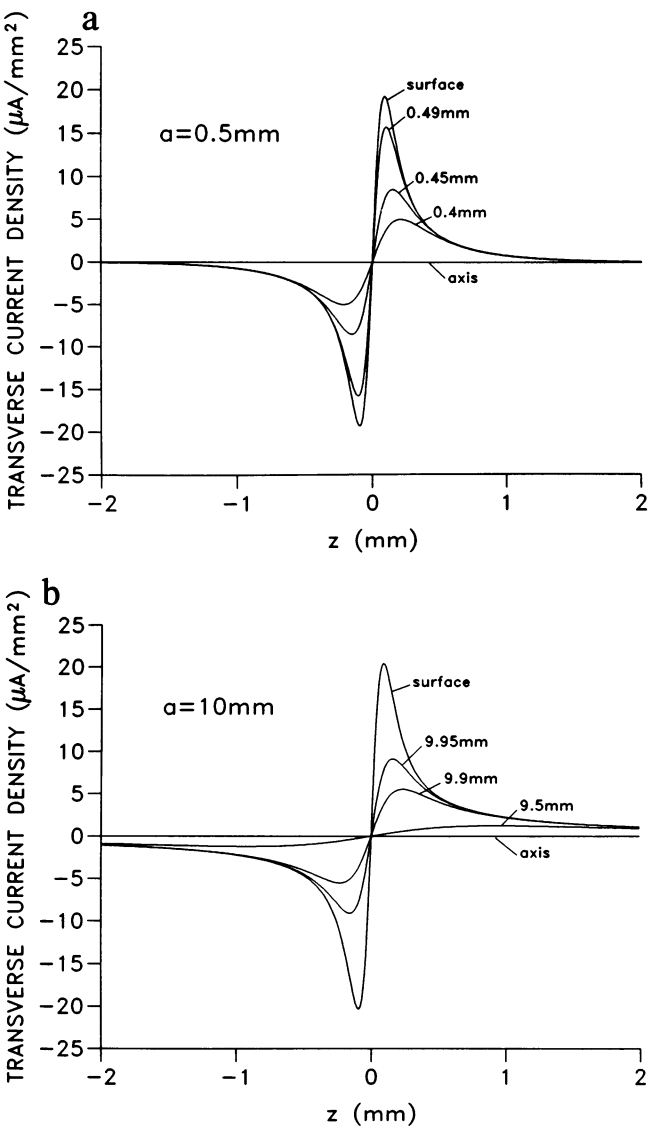


FIGURE 4 Plot of interstitial transverse current density vs. axial distance, $z$, at different depths in a cylindrical bidomain with a radius of (*a*) 0.5 mm and (*b*) 10.0 mm.

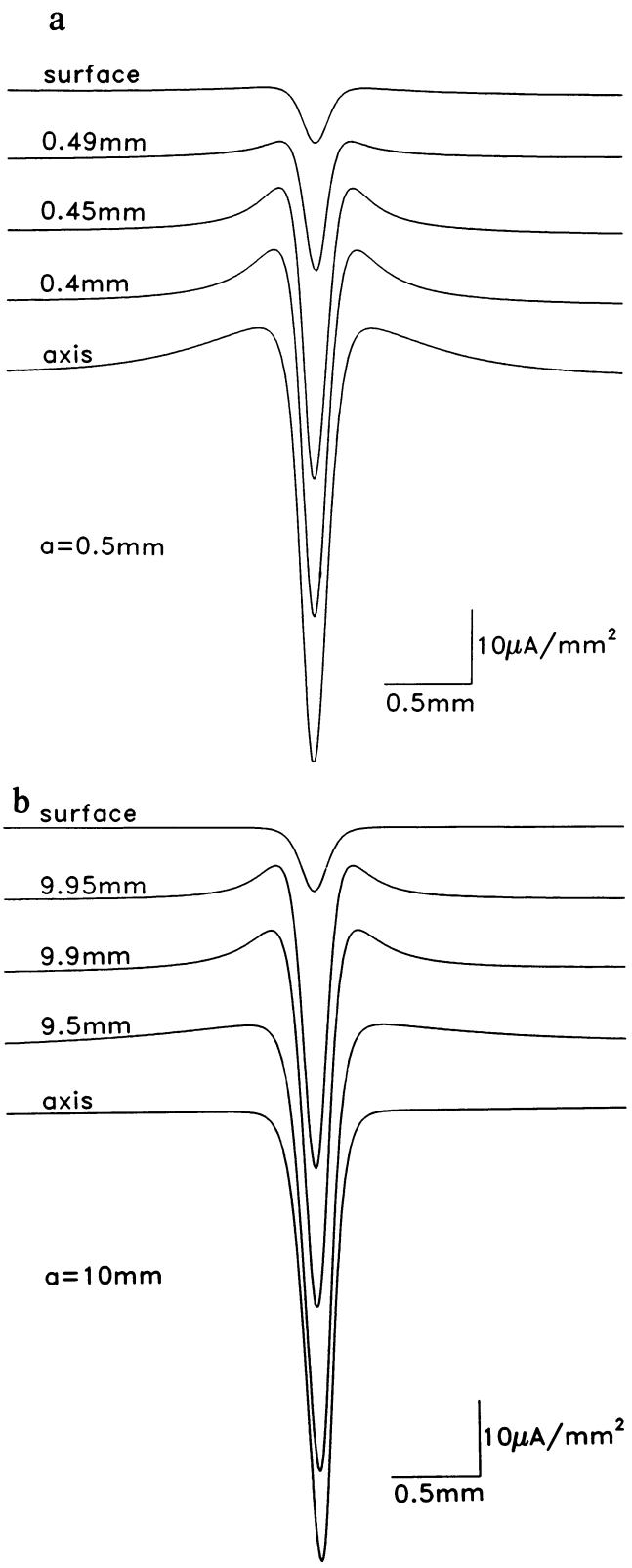


FIGURE 5 Plot of longitudinal current density vs. axial distance, $z$, at different depths in a cylindrical bidomain with a radius of (*a*) 0.5 mm and (*b*) 10.0 mm. Note that the ends of each curve can be taken to be the origin of the ordinate axis. The origin of the $z$-axis is at the peak negative deflection.

here, indicate the direction (denoted by arrows) but not the magnitude of the total current density at each field point. Note that because the current density in the interstitial space, $\mathbf{J}_e$, is not solenoidal ($\nabla \cdot \mathbf{J}_e \neq 0$), the number of the flow lines per unit area cannot be interpreted as proportional to the magnitude of $\mathbf{J}_e$, and therefore no attempt was made to indicate the magnitude in Figs. 7 *b* and 8 *b*. Within the active region, the field is primarily axial with some fringing near the surface. In the 0.5-mm bundle, there is a large radial component to the field outside the active region. The interstitial current throughout the cross-section flow directly into the extracellular conducting medium. In contrast, only interstitial current from the region <1 mm below the surface of the large bundle flow into the extracellular space. Near the center of the large bundle, the interstitial current flow is primarily axial. The

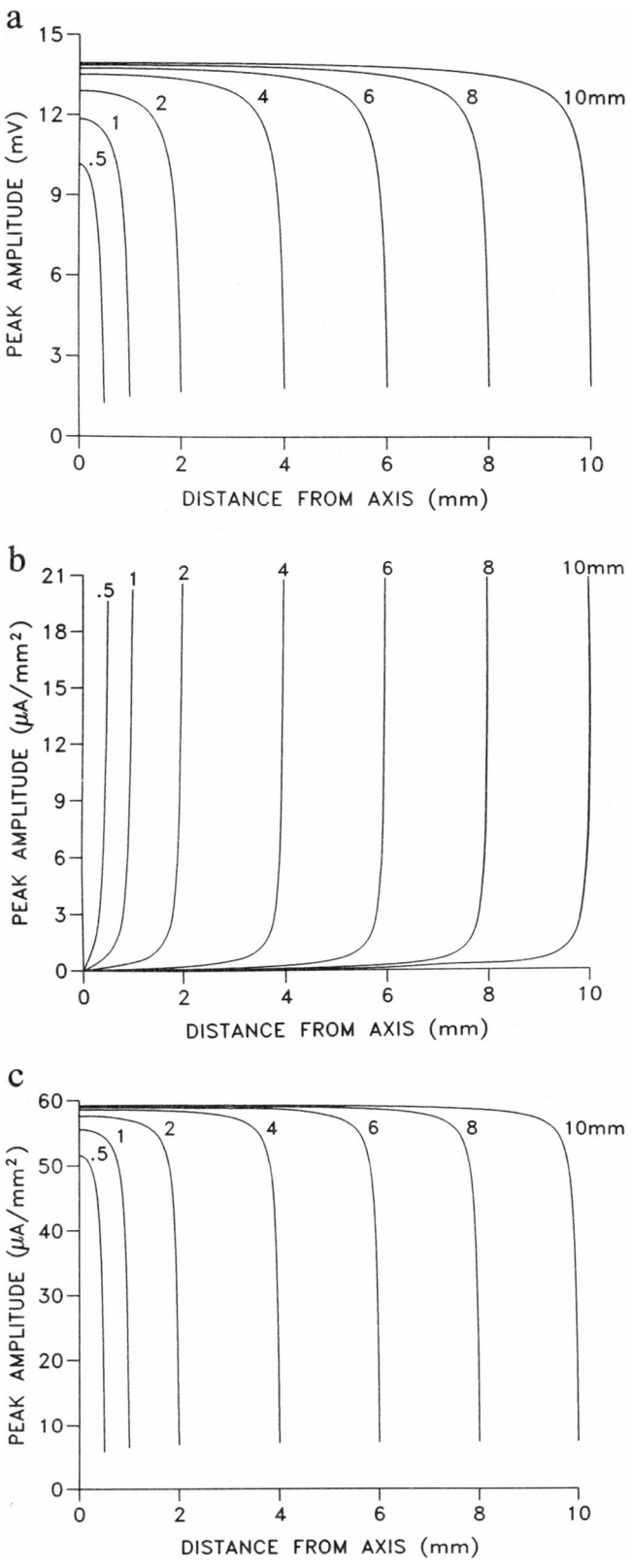


FIGURE 6 Plot of the peak amplitude in interstitial (*a*) potential, (*b*) transverse current density, and (*c*) longitudinal current density vs. radial distance from the axis for a series of bundle radii (0.5, 1, 2, 4, 6, 8, and 10 mm). In *a* and *b*, peak amplitude refers to positive peak amplitude, whereas in *c* peak amplitude refers to negative peak amplitude.

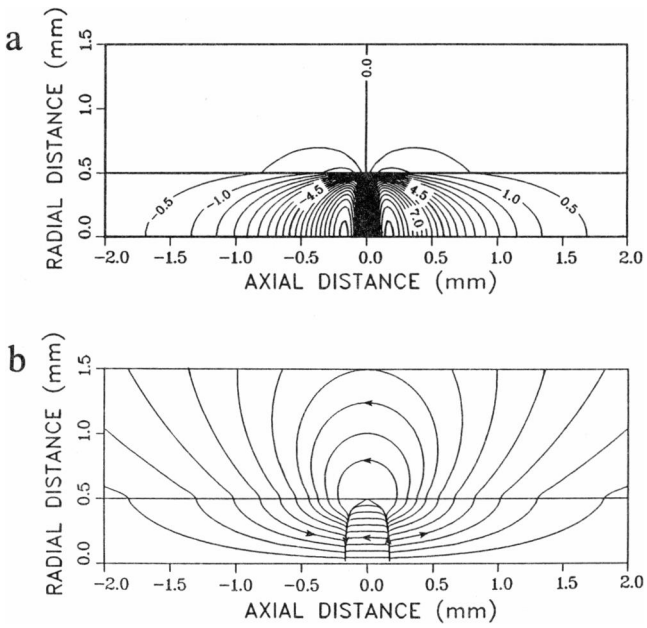


FIGURE 7 (*a*) Equipotential plot of the interstitial and extracellular potential and (*b*) a plot of the interstitial and extracellular current flow lines in and near the region of the rising phase of $V_m$ from activity in a cylindrical bidomain of radius 0.5 mm. The current flow lines indicate the direction (*arrows*) but not the magnitude of the total current density at each field point.

direction of the currents inside and outside the active region corresponds to the triphasic shape of the longitudinal current density. The radial current corresponding to the crest in the equipotential lines is consistent with the biphasic shape of the transverse current density. The magnitude of this current increases as it approaches the surface. In both bundles, the notch in the current flow lines at the surface reflects the discontinuity in the longitudinal current density. Note that because of the anisotropy, the equipotential lines and current flow lines are not orthogonal inside the bundle.

Finally, in Fig. 9 the surface potential of a 0.5-mm bundle modeled as a cylindrical bidomain is compared with the surface potential of a bundle modeled as a single fiber with $\sigma_i = g_{iz}/f_i$. For completeness, the field from the single fiber is evaluated in two ways: from the expressions (Eq. 36) derived from solving Laplace's equation in cylindrical coordinates (curve *1*), and from expressions (Eq. 40) assuming the source is concentrated on the axis (curve *2*). For the given set of parameters, the potentials predicted by the single fiber are clearly different from that predicted from the cylindrical bidomain (curve *3*). The difference of the line source solution from the rigorous single fiber solution (magnitude and axial extent) reflects a fundamental limitation of the line source for describing fields generated by large fibers when $V_m(z)$ is that of a smaller component fiber.

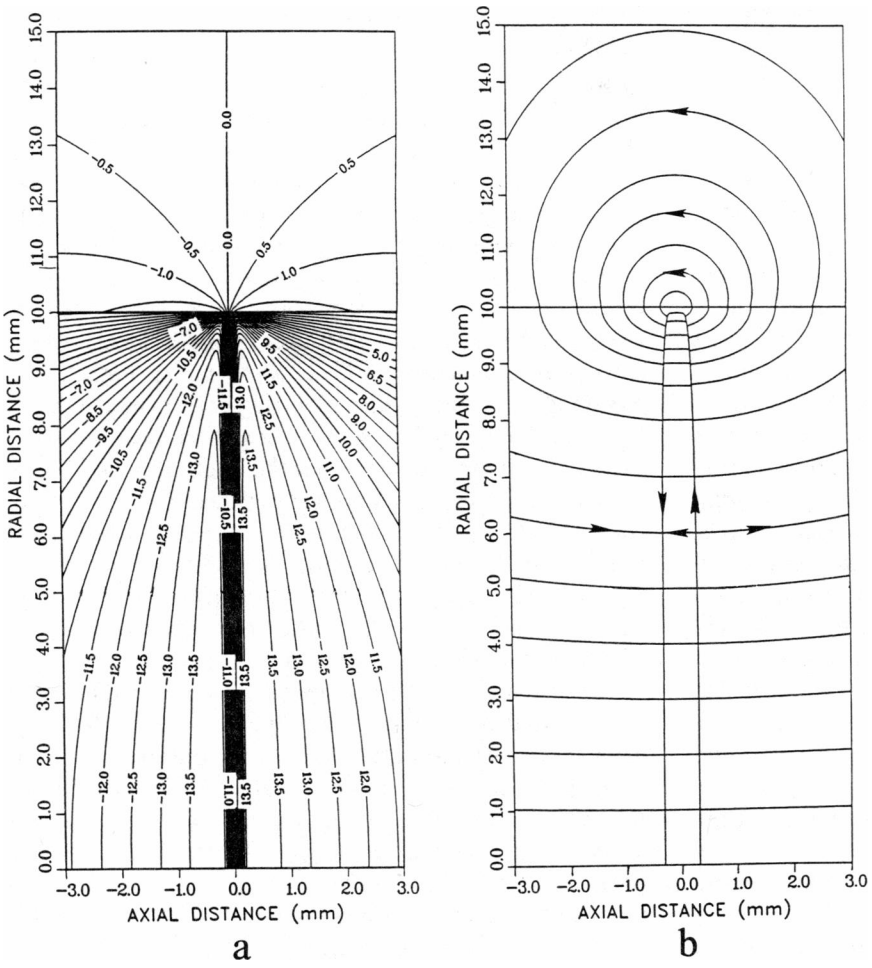


FIGURE 8 (*a*) Equipotential plot of interstitial and extracellular potential and (*b*) a plot of the interstitial and extracellular current flow lines from activity in a cylindrical bidomain of radius 10.0 mm. In contrast to the 0.5 mm bundle, only interstitial current from the more superficial tissue flows directly into the extracellular volume conductor. The tissue near the center of the bundle appears to contribute only an axial current in accordance with linear core-conductor behavior.

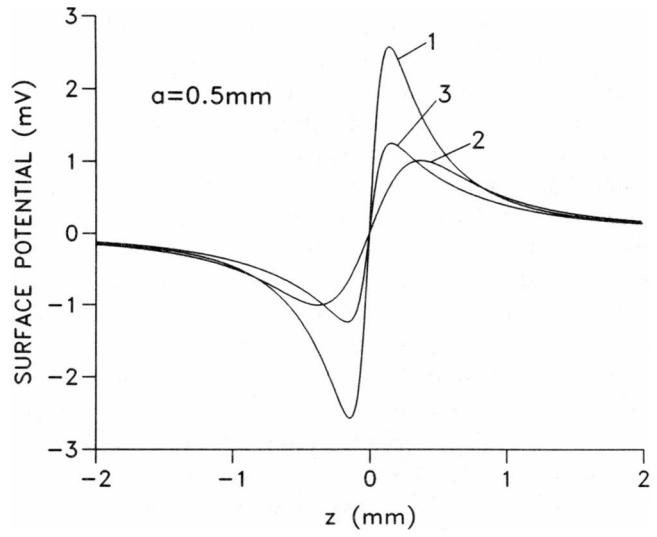


FIGURE 9 Comparison of the surface potential in a 0.5 mm bundle modeled as an equivalent single fiber (curves *1* and *2*) with $\sigma_i = g_{iz}/f_i$ and as a cylindrical bidomain (curve *3*). The surface potential for the single fiber is calculated using two methods: from expressions derived from solving Laplace's equation in cylindrical coordinates (curve *1*) and from the line source expression (curve *2*).

## DISCUSSION

A simple view of a multicellular preparation is to assign each fiber an axial source density given by (17)

$$\frac{\partial^2}{\partial z^2}(\sigma_e\Phi_e - \sigma_i\Phi_i). \tag{45}$$

Since $\Phi_e$ and $\Phi_i$ are functions of $\rho$ and $z$, the source density is not uniform throughout any cross-section. The evaluation of the space averaged potential distribution from the bidomain equations indicates that source density is greatest near the axis and smallest near surface. The magnitude and radial variation depend on the radius of bundle, the conductivity values of both domains, and $V_m(\rho, z)$. For a very large bundle, an ideal central fiber can be approximated by a core-conductor fiber, while an ideal surface fiber can be approximated by an isolated fiber. By substituting Eqs. 42 and 43 for $\Phi_e$ and $\Phi_i$ in Eq. 45 above, the source density of an ideal central fiber can be shown to be proportional to

$$\left(\frac{\sigma_e\sigma_i}{\sigma_e f_e + \sigma_i f_i}\right)\frac{\partial^2 V_m}{\partial z^2}, \tag{46}$$

while the source density of an ideal surface fiber is proportional to

$$\sigma_i \frac{\partial^2 V_m}{\partial z^2}. \quad (47)$$

Hence for typical values of conductivity (i.e., $\sigma_i/\sigma_e < 1.0$), the source strength of a central fiber is greater by a factor of $1/(1 - \alpha f_i)$, where $\alpha = 1 - \sigma_i/\sigma_e$.

If the rising phase of the action potential is approximated to be linear, then the source actually consists of a positive disk at the site where depolarization begins and a negative disk at the site where depolarization ends (beginning of plateau). In the bidomain model, each of these single source surfaces extends across the fiber bundle forming a circular source lamina. Since $\Phi_e$ and $\Phi_i$ depend on the distance from the axis, the circular lamina sources have a strength that depends on the distance from the axis, as discussed earlier. The gross behavior of the field generated by the positive and negative source lamina described above corresponds to that seen in the figures here. The field is greatest between the lamina, since the two sources set up a field in the same direction, and is primarily axial. Outside the lamina, but within the bundle, the field is also axial but with lower intensity. In these regions the positive and negative sources set up opposing fields. This field is directed away from the positive lamina, accounting for the ridge for current flow seen in Figs. 7 and 8.

In Figs. 7 *b* and 8 *b* it appears as if the central fibers contribute only an interstitial current. However, the electric field set up by each fiber in the preparation affects the currents throughout the interstitial and extracellular space. The total field due to activity in the bundle is a superposition of the individual fields of the component fibers. The direction of that field and currents depends on the site of evaluation. Near the axis the electric fields superimpose to produce a field and total current density with a direction predominantly parallel to the axis. The magnitude of field is greatest at the axis because the partial fields from each source element tends to add in the same direction. Approaching the surface the radial component of the total field and current density increases and the magnitude of the field decreases.

As noted above, the field of a bundle modeled as a bidomain can be treated as a superposition of the fields generated by separate fibers. This treatment has been used by a number of electrophysiologists in their investigations of the behavior of nerve and muscle bundles (2, 3, 5). However, in most of these bundle representations the interstitial potential is ignored, and the field is modeled as a linear summation of the fields of independent single fibers in an unbounded volume conductor with some spatial distribution. This failure to include the interstitial potential as part of the overall source density may lead to erroneous conclusions about the preparation such as the effect of variation in the number of fibers in a bundle or the magnitude of the extracellular potential.

An alternative and equivalent source model for the bundle is the single fiber described by Eqs. 36 and 37. The equivalent single fiber has the same radius as the bundle but requires intracellular and extracellular conductivities that depend on the four conductivity values characterizing the three domains. In addition, an amplitude factor, involving the axial bidomain conductivities, must be applied to the single equivalent fiber solution. Clearly, the common approach (4) of assigning a value to the intracellular conductivity equal to the axial intracellular conductivity of the preparation (i.e., $\sigma_i = g_{iz}/f_i$) does not necessarily lead to a valid equivalent single fiber, as shown in Fig. 9. One advantage to using an equivalent single fiber model rather than the equivalent fiber sources of a cylindrical bidomain to model an entire bundle is that the single fiber behavior is relatively familiar and more simply described. For example, the field can be thought of as arising from stacks of uniform single layer disks with a strength proportional to $\partial^2/\partial z^2$ ($\sigma_e\Phi_e - \sigma_i\Phi_i$) evaluated at the surface only. A more detailed examination of the difference between these two models is the subject of a subsequent study.

The bidomain model enables the analytic evaluation of the potential distribution in the bundle because the intracellular and extracellular spaces are considered as continua. For the arbitrary but reasonable choice of conductivity values used here, we find that the core-conductor approximation is adequate only in the region of the rising phase of $V_m$ for fibers near the center of a bundle with a radius greater than 10 times the axial extent of $V_m$. If the wavefront were propagating with a velocity of 0.25 m/s (rather than the assumed 0.50 m/s), then we would expect to see core-conductor behavior near the center of a bundle with a radius of 5 mm (vs. 10 mm). In fact, core-conductor behavior characterizes 90% of the cross-section. For smaller bundles, the peak potential is smaller than that predicted by a core-conductor model but still large enough to affect the overall source density. The simulations also demonstrate that the results from the semi-infinite block studied by Plonsey and Barr (8) cannot be easily extrapolated to a radially finite cylindrical bidomain. In principle, their results apply only when the radius approaches infinity. Although the greatest change in potential occurs between the surface and a depth of 0.5 mm, the shape and magnitude depend on the bundle size.

Finally, we assumed that the propagating wavefront was planar and traveling with uniform velocity. In real preparations, particularly striated muscle or nerve bundles, this assumption may not always be justified since the variation in the behavior of the interstitial potentials with depth influences the velocity and can cause dispersion. There is some evidence (18) that suggests that the activation profile in a cardiac fiber bundle is curved, with activity at the surface leading in phase that at the center. This curved phase front is likely to propagate at a uniform velocity that is determined by the electrical properties characterizing the bulk of the cross-section (19). The radial potential

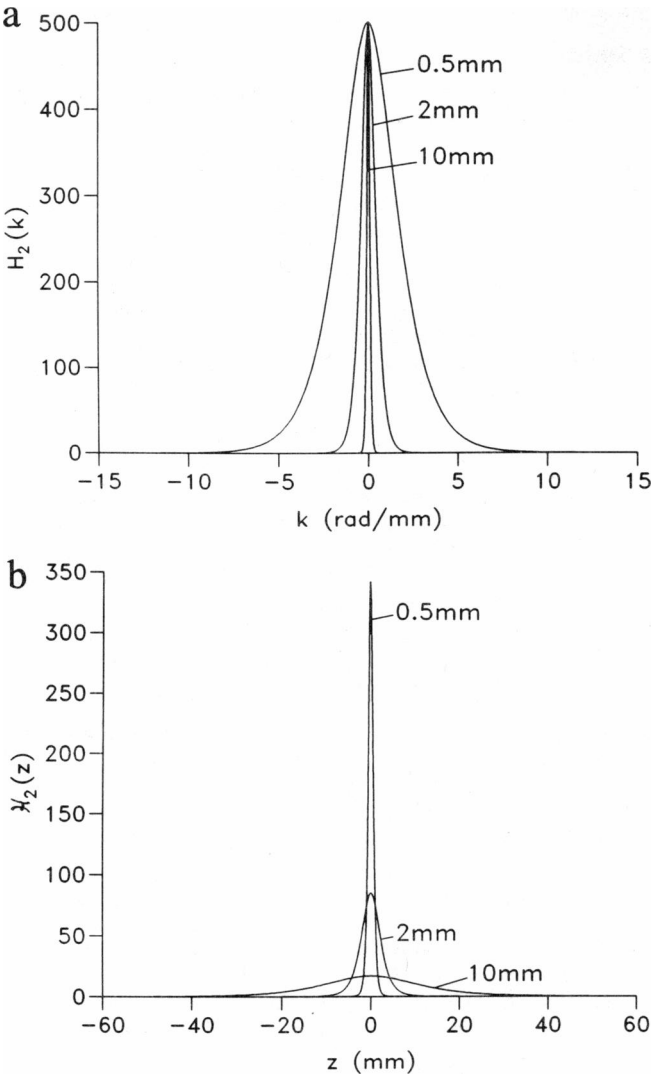


FIGURE 10 (*a*) Plot of the filter function $H_2(k)$ and (*b*) its Fourier transform, $\mathcal{H}_2(z)$, at the axes of three bundles with radii 0.5, 2.0, and 10 mm.

gradient set up by such a wavefront will lead to a redistribution of currents from the periphery to the center of the bundle, resulting in fields different from those generated by planar activation. Unfortunately, the exact details of the phase variation are not known, so the effect of the deviation from planar behavior cannot be fully elucidated.

## APPENDIX

The behavior of the interstitial potential at the axis ($\rho = 0$) depends on a number of factors including the extent of the rising phase, the conductivities, the total duration of the action potential, and the radius of the bundle. We can examine the effect of the latter two parameters on the potentials through application of the convolution theorem. This permits rewriting Eq. 15 as

$$\Phi_e(\rho, z) = C(z) - D(z), \tag{A1}$$

where

$$C(z) = \sigma_o \frac{g_{iz}}{g_{iz} + g_{ez}} \int_{-\infty}^{\infty} V_m(\tau)\, \mathcal{H}_2(z - \tau)\, d\tau \tag{A2}$$

and

$$D(z) = \frac{g_{iz}}{g_{iz} + g_{ez}} V_m(z), \tag{A3}$$

and $\mathcal{H}_2(z)$ is the filter response in the $z$-domain.

As shown in Fig. 10 *a*, the filter $H_2(k)|_{\rho=0}$ acts as a low pass filter with a constant peak amplitude, $1/\sigma_o$. As the radius of the bundle increases, the cut-off frequency decreases. Correspondingly in the $z$-domain (Fig. 10 *b*), $\mathcal{H}_2(z)$ becomes broader, as the bundle radius increases, but reduced in amplitude such that the total area remains constant and equal to $1/\sigma_o$.

Fig. 11 graphically illustrates the evaluation of Eq. A1. Each vertical column (panel) plots the same functions under the different conditions established in rows *a–c*. The relative magnitudes and extents of the functions to be convolved, $V_m(z)$ and $\mathcal{H}_2(z)$ (*shaded curve*), are shown in *A*. $C(z)$, the result of the convolution multiplied by the constant $\sigma_o g_{iz}/(g_{iz} + g_{ez})$ (*solid curve*), and the negative of the core-conductor potential,

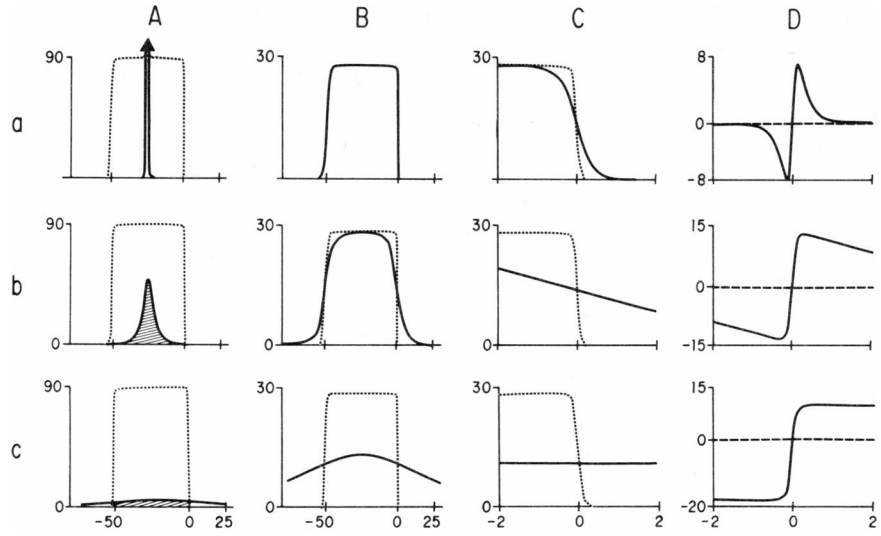


FIGURE 11 Graphical evaluation of Eq. A1. Each vertical column (panel) plots the same functions under the different conditions established in rows *a–c* (see text for details). The abscissa of each plot is in the units of millimeters. The relative magnitudes and extents of the functions $V_m(z)$ (mV) and $\mathcal{H}_2(z)$ (mm/S) (*shaded curve*) are shown in *A*. $C(z)$ (mV), the result of the convolution multiplied by the constant $\sigma_o g_{iz}/(g_{iz} + g_{ez})$ (*solid curve*), and the negative of the core-conductor potential, $D(z)$ (mV) (*dashed curve*), are shown in *B*. *C* is a reproduction of *B* in the region of the rising phase (symmetric about 0 mm). Finally, the interstitial potential, $\Phi_e(0, z)$ (mV), computed from Eq. A1 is shown in *D*. Note that the units have been deliberately left off the axes to simplify the figure.

$D(z)$ (*dashed curve*), are shown in *B*.[5] *C* is a reproduction of *B* in the region of the rising phase (symmetric about 0 mm). Finally, the interstitial potential, $\Phi_e(0, z)$, computed from Eq. A1 is shown in *D*.

For the case of a bundle with a small radius (Fig. 11 *a*), the function $\mathcal{H}_2(z)$ is very sharp. As shown in *B*, $C(z)$ is a smoothed version of the negative of the core-conductor potential, $D(z)$.

Over most of the plateau of the cardiac action potential ($z_1$ to $z_2$), where $V_m(z)$ has a nearly constant peak amplitude of $\hat{V}_m$,

$$C(z) = \sigma_o \frac{g_{iz}}{g_{iz} + g_{ez}} \hat{V}_m \int_{z_1}^{z_2} \mathcal{H}_2(z - \tau)\, d\tau = \frac{g_{iz}}{g_{iz} + g_{ez}} \hat{V}_m. \quad \text{(A4)}$$

In the region just outside the rising phase, the difference between $C(z)$ and $D(z)$ is zero. The resulting potential, $\Phi_e$, is biphasic, symmetric, and centered about 0 mV.

As the radius increases, the axial interstitial potential in the region of the rising phase approaches the ideal core-conductor potential (Eq. 27) in both shape and magnitude but with some "offset." (The term offset refers to the amount needed to shift the ideal core-conductor potential so that the shape and magnitude can be compared with $\Phi_e$ in the region of the rising phase.) The offset is determined by the relative extents of $V_m(z)$ and $\mathcal{H}_2(z)$.

In Fig. 11 *b* the radius is large enough to produce approximate core-conductor behavior, however, the potential is still centered about 0 mV. This offset results because the extent of $\mathcal{H}_2(z)$ is smaller than the extent of the plateau of $V_m(z)$ and, as is the case for the small bundle, the peak amplitude of $C(z)$ is equal to the peak amplitude of $D(z)$.

In Fig. 11 *c* the radius is increased such that the extent of the filter in the $z$-domain is larger than the extent of $V_m(z)$. In the plateau phase,

$$\int_{z_1}^{z_2} \mathcal{H}_2(z - \tau)\, d\tau < \frac{1}{\sigma_o}. \quad \text{(A5)}$$

Therefore, the peak amplitude of $C(z)$ is smaller than $D(z)$, and $\Phi_e$ is no longer centered about 0 mV. In the limit ($a \to \infty$), $C(z)$ is zero, and $\Phi_e$ is exactly equal to the core-conductor potential (Eq. 27).

This research was supported by the Department of Biomedical Engineering, Duke University and by grants HL-11307 from the National Institutes of Health and ECE-85-14278 from the National Science Foundation.

*Received for publication 7 October 1987 and in final form 18 January 1988.*

## REFERENCES

1. Ganapathy, N., J. W. Clark, Jr., O. B. Wilson, and W. Giles. 1985. Forward and inverse potential field solutions for cardiac strands of cylindrical geometry. *IEEE (Inst. Electr. Electron. Eng.) Trans. Biomed. Eng.* 32:566–577.
2. Nandedkar, S., and E. Stalberg. 1983. Simulation of macro EMG motor unit potentials. *Electroencephalogr. Clin. Neurophysiol.* 56:52–62.
3. Schoonhoven, R., D. F. Stegemen, and A. Van Oosterom. 1986. The forward problem in electroneurography II: comparison of models. *IEEE (Inst. Electr. Electron. Eng.) Trans. Biomed. Eng.* 33:335–341.
4. Spach, M. S., and P. C. Dolber. 1986. Relating extracellular potentials and their derivatives to anisotropic propagation at a microscopic level in human cardiac muscle. *Circ. Res.* 58:356–371.
5. Stegeman, D. F., J. P. C. De Weerd, and E. G. J. Eijkman. 1979. A volume conductor study of compound action potentials of nerves in situ: The forward problem. *Biol. Cybern.* 33:97–111.
6. Sommer, J. R., and B. Scherer. 1985. Geometry of cell and bundle appositions in cardiac muscle: light microscopy. *Am. J. Physiol.* 248:H792–H803.
7. Roth, B. J., and J. P. Wikswo, Jr. 1986. A bidomain model for the extracellular potential and magnetic field of cardiac tissue. *IEEE (Inst. Electr. Electron. Eng.) Trans. Biomed. Eng.* 33:467–469.
8. Plonsey, R., and R. C. Barr. 1987. Interstitial potentials and their change with depth into cardiac tissue. *Biophys. J.* 51:547–555.
9. Tung, L. 1978. A bidomain model for describing ischemic myocardial d-c potentials. Ph.D. dissertation. Massachusetts Institute of Technology, Cambridge. pp. 59-102.
10. Henriquez, C. S., and R. Plonsey. 1987. Effect of resistive discontinuities on velocity and waveshape in a single cardiac fibre. *Med. Biol. Engr. Comp.* 25:428–438.
11. Rudy, Y., and W. Quan. 1987. A model study of the effects of the discrete cellular structure on electrical propagation in cardiac tissue. *Circ. Res.* 61:815–823.
12. Clerc, L. 1976. Directional differences of impulse spread in trabecular muscle from mammalian heart. *J. Physiol. (Lond.).* 255:335–346.
13. Plonsey, R. 1974. The active fiber in a volume conductor. *IEEE (Inst. Electr. Electron. Eng.) Trans. Biomed. Eng.* 21:371–381.
14. Plonsey, R. 1969. Biolectric Phenomena. McGraw-Hill Book Co., New York. pp. 202–275.
15. Hodgkin, A. L., and W. A. H. Rushton. 1946. The electrical constants of crustacean nerve fiber. *Proc. R. Soc. Lond. Biol. Sci.* 133:444–479.
16. Press, W. H., B. P. Flannery, S. A. Teukolsky, and W. T. Vetterling. 1986. Numerical Recipes. Cambridge University Press, Cambridge, UK. pp. 381–453.
17. Plonsey, R. 1984. Quantitative formulation of electrophysiological sources of potential fields in a volume conductor. *IEEE (Inst. Electr. Electron. Eng.) Trans. Biomed. Eng.* 31:868–872.
18. Suenson, M. 1985. Interaction between ventricular cells during the early part of excitation in ferret heart. *Acta. Physiol. Scand.* 125:81–90.
19. Plonsey, R., C. S. Henriquez, and N. Trayanova. 1988. Extracellular (volume conductor) effect on adjoining cardiac muscle electrophysiology. *Med. Biol. Engr. Comp.* In press.

[5]To facilitate the comparison of waveshapes, the *negative* of the ideal core-conductor potential (Eq. 27) is plotted in *B* and *C*.